ACES Asian Chemical Editorial Society

doi.org/10.1002/asia.70245

CHEMISTRY
AN ASIAN JOURNAL
Research Article

www.chemasianj.org

Fused Dithienoheterocycle-Based Hole-Transporting Materials for Efficient Perovskite Solar Cells

Kun-Mu Lee,[a, b, c, d] Wei-Hao Chiu†,[b] Bo-Chin Lee†,[e] Yu-Hsin Kao,[e] Jr-Si Hsu,[e] and Yung-Sheng Yen*[e]

The development of efficient and stable hole-transporting materials (HTMs) is critical for advancing perovskite solar cell (PSC) technology. This study presents two novel HTMs, **LK-1** and **LK-2**, based on fused dithienoheterocycle derivatives, namely, dithieno[3,2-*f*:2′,3′-*h*]quinoxaline (DTQu) and dithieno[3,2-*a*:2′,3′-*c*]phenazine (DTPh), designed for PSCs. These donor–acceptor–donor (D–A–D) structured HTMs exhibit planar, rigid cores that enhance π–π stacking, improving hole mobility and stability. **LK-1** and **LK-2** were synthesized and characterized for their optical, electrochemical, and thermal properties. PSCs with **LK-1** achieved a power conversion efficiency (PCE) of 18.16%, whereas **LK-2** reached 19.40%, outperforming **LK-1** due to smoother film properties and reduced recombination. Both HTMs showed high thermal stability and suitable energy alignment with the perovskite layer. **LK-2**-based PSCs enhanced hydrophobicity and film morphology further suggest its potential for stable, efficient PSCs, advancing the development of robust organic HTMs.

1. Introduction

In recent years, with the growing global energy demand and concerns about environmental issues, pursuing sustainable energy solutions has become more imperative. Perovskite solar cells (PSCs) have rapidly ascended as a front-running contender in photovoltaic technology, largely attributable to their remarkable power conversion efficiencies (PCEs) and the potential for cost-effective fabrication.[1–3] PSCs have demonstrated remarkable progress, with the current highest power conversion efficiency (PCE) reaching over 26%.[4–7] Hole-transporting materials (HTMs) are integral components of efficient PSCs, facilitating the extraction and transport of positively charged carriers (holes) generated within the perovskite absorber layer to the charge-collecting electrode.[8] Among the diverse classes of HTMs, organic small molecular HTMs have garnered considerable interest and numerous small molecule HTMs have been developed in recent years.[9–16] This interest stems from their well-defined chemical structures, which enable precise control over their electronic properties through rational molecular design, coupled with facile synthesis and purification routes. Furthermore, many organic small molecules are amenable to solution processing techniques, facilitating the fabrication of thin-film devices via scalable and cost-effective methods.[17,18] Currently, the most widely used small molecule HTM is spiro-OMeTAD (2,2′,7,7′-tetrakis[*N*,*N*-di(4-methoxyphenyl)amino]-9,9′-spirobifluorene),[19,20] which has relatively low hole mobility and requires the use of additives to enhance its performance.[21,22] Unfortunately, the additives can induce device degradation due to their inherent sensitivity to moisture and propensity to volatilize over time, thereby compromising the long-term operational stability of the PSC. Consequently, the exploration of alternative, economically viable, and robust organic small molecule HTMs capable of overcoming the aforementioned limitations associated with spiro-OMeTAD.

Recent research has focused on developing novel HTMs with planar fused-heterocyclic cores to improve both efficiency and stability.[23,24] For example, Santos et al. reported an anthradithiophene-based HTM, named ADT-TPA, that achieved a PCE of 17.60% under AM 1.5 G illumination.[25] In 2024, Wagner and coworkers designed a T-shaped coplanar π-extended quinoxaline-based HTM that demonstrated a PCE of 20.39% in dopant-free PSCs and exhibited excellent long-term stability, retaining 95% of its initial PCE after 500 h.[26] Chen's group reported a series of electron-rich fused-heterocyclic HTMs based on a dithienothiophenepyrrole core, achieving a PCE of over 23% in PSCs.[27] These examples highlight the potential of rigid, planar, fused-heterocyclic cores in developing high-performance and stable HTMs for PSCs. Therefore,

[a] *K.-M. Lee*
Department of Chemical and Materials Engineering, Chang Gung University, Taoyuan 33302, Taiwan

[b] *K.-M. Lee, W.-H. Chiu†*
Center for Green Technology, Chang Gung University, Taoyuan 33302, Taiwan

[c] *K.-M. Lee*
Division of Neonatology, Department of Pediatrics, Chang Gung Memorial Hospital, Linkou, Taoyuan 33305, Taiwan

[d] *K.-M. Lee*
College of Environment and Resources, Ming Chi University of Technology, New Taipei City 24301, Taiwan

[e] *B.-C. Lee†, Y.-H. Kao, J.-S. Hsu, Y.-S. Yen*
Department of Chemistry, Chung Yuan Christian University, Zhongli, Taoyuan 320, Taiwan
E-mail: ysyen@cycu.edu.tw

[†] *Both authors equally contributed to this work.*

Supporting information for this article is available on the WWW under https://doi.org/10.1002/asia.70245

exploring different rigid conjugated cores and their applications in HTMs is crucial for advancing the field of PSCs. In this context, the incorporation of rigid and planar dithieno-fused heterocyclic conjugated cores within the molecular architecture of novel small molecule HTMs represents a promising strategy for enhancing device performance and stability.

With our continuing interest in polyarene-based HTMs for PSCs,[28–30] thereby we present two HTM molecules with donor–acceptor–donor (D–A–D) conjugated structures **LK-1** and **LK-2** that are the utilization of dithieno[3,2-*f*:2′,3′-*h*]quinoxaline (DTQu) and dithieno[3,2-*a*:2′,3′-*c*]phenazine (DTPh) as central conjugated building blocks. The quinoxaline-based derivatives were promising building entities in high performance optoelectronic materials,[31–34] notably offering cost-effectiveness, and allowing for easy chemical modifications on its pyrazine heterocycle. Recently, DTQu and DTPh have been demonstrated as effective π-conjugated building blocks for the construction of highly efficient HTM for PSCs applications.[33,35,36] These fused core structures were designed by fusing two thiophene rings with a central nitrogen-containing quinoxaline, possess rigid and planar characteristics. This planarity facilitates stronger π–π stacking interactions,[37–40] and enriched intermolecular interactions, which are beneficial for enhancing hole mobility and overall device performance. These structures provide a versatile platform for modulating electronic properties and promoting intermolecular interactions. Furthermore, the presence of nitrogen heteroatoms within the quinoxaline and phenazine units can play a beneficial role in passivating defects within the perovskite layer. These nitrogen atoms can act as Lewis bases, coordinating with undercoordinated lead ions (Pb^{2+}) on the perovskite surface, thereby reducing trap states and improving the overall quality of the perovskite film.[41–44] On the other hand, introducing the alkoxy chain into the structure not only improves the solubility and enhances hydrophobicity, but also may shorten the π–π stacking distance and reduce defects.[45–47] The electron-deficient nature of the quinoxaline and phenazine units enables the modulation of the highest occupied molecular orbital (HOMO) energy levels, enhancing stability and reducing the energy mismatch with the perovskite valence band. Through strategic integration of these cores with suitable donor moieties, it becomes feasible to design D–A–D structured HTMs capable of promoting efficient charge transport and extending device longevity. Furthermore, the use of electron-deficient cores in D–A–D structures can also promote favorable molecular packing and morphology, which is essential for efficient charge transport, as the interactions between the molecules, such as π–π stacking, can be influenced by the choice of donor and acceptor units, leading to enhanced hole mobility.[48–50] In this work, we introduce and systematically study the influence of HTMs featuring two distinct fused dithiophene heterocyclic cores, DTQu and DTPh, on the PCE of PSCs. As a result, PSCs utilizing **LK-2** as HTM achieve a maximum PCE of 19.40%, which is higher than that of devices using **LK-1** (18.16%). Furthermore, the high hydrophobic nature of our HTMs exhibits improved long-term stability for **LK-2**-PSCs, maintaining 81% retention after 1000 h in comparison with spiro-OMeTAD-based PSCs.

2. Results and Discussion

2.1. Synthesis of the Materials

The synthesis procedure and the molecular structures are outlined in Scheme 1. The starting materials **3** and **4** were synthesized from benzo[2,1-*b*:3,4-*b*′]dithiophene-4,5-dione (**1**), which was prepared according to the procedure reported in the literature.[51] First, compound **1** reacts with hydroxylamine hydrochloride to form dioxime, and then the dioxime is reduced to compound **2** using palladium/activated carbon and hydrazine. Subsequently, compound **3** was obtained by a condensation reaction between 1,2-bis(4-methoxyphenyl)ethane-1,2-dione and compound **2** in good yields.[51] On the other hand, compound **1** reacts with 4,5-bis(hexyloxy)benzene-1,2-diamine in refluxing ethanol to afford the desired compound **4** in moderate yields. The final target molecules, **LK-1** and **LK-2**, were then synthesized by reacting boron ester compound **5** with **1** and **2** via Suzuki–Miyaura coupling reaction, respectively.

2.2. Optical Properties

The optical absorption properties of **LK-1** and **LK-2** were measured in CH_2Cl_2 solution by UV–vis spectrometer. Figure 1 displayed the absorption spectra of **LK-1** and **LK-2** and the corresponding data were listed in Table 1. The absorption spectra of **LK-1** and **LK-2** have two primary absorption peaks. The absorption peak in the range of 350 to 450 nm is speculated to be a localized π–π^* electron transition, whereas the other absorption peak in the range of 450 to 550 nm is intramolecular charge transfer (ICT), which is the electron transfer from the peripheral TPA donor to the electron-deficient core. The absorption maximum of **LK-1** and **LK-2** were 457 and 492 nm, respectively. The DTQu and DTPh used in **LK-1** and **LK-2** were electron-deficient heterocyclic conjugation molecules, which facilitating induce ICT for D–A–D type structure configuration. Obviously, the absorption maximum of dithieno[3,2-*a*:2′,3′-*c*]phenazine-based **LK-2** was red-shifted compared to that of **LK-1**. It is expected that DTPh is a stronger electron-withdrawing entity than DTQu. Moreover, the optical band gaps of **LK-1** and **LK-2** were calculated to be 2.41 and 2.29 eV, respectively, from the intersection of normalized UV–vis absorption and fluorescence spectra. The fluorescence properties of these two molecules were investigated, as shown in Figure 1. The emission maximum of **LK-1** and **LK-2** were 590 and 624 nm with larger Stokes shifts (>4000 cm^{-1}), respectively, which provided supporting evidence for ICT characteristic and was consistent with the trend of absorption. The absorption spectra in the thin-film state of **LK-1** and **LK-2** were shown in Figure S1. In the thin-film state, the two major prominent absorption bands were red-shifted slightly and broadened with respect to those in solution. This was due to the intermolecular π–π stacking interaction in the films, which may be beneficial to improve the charge transport.

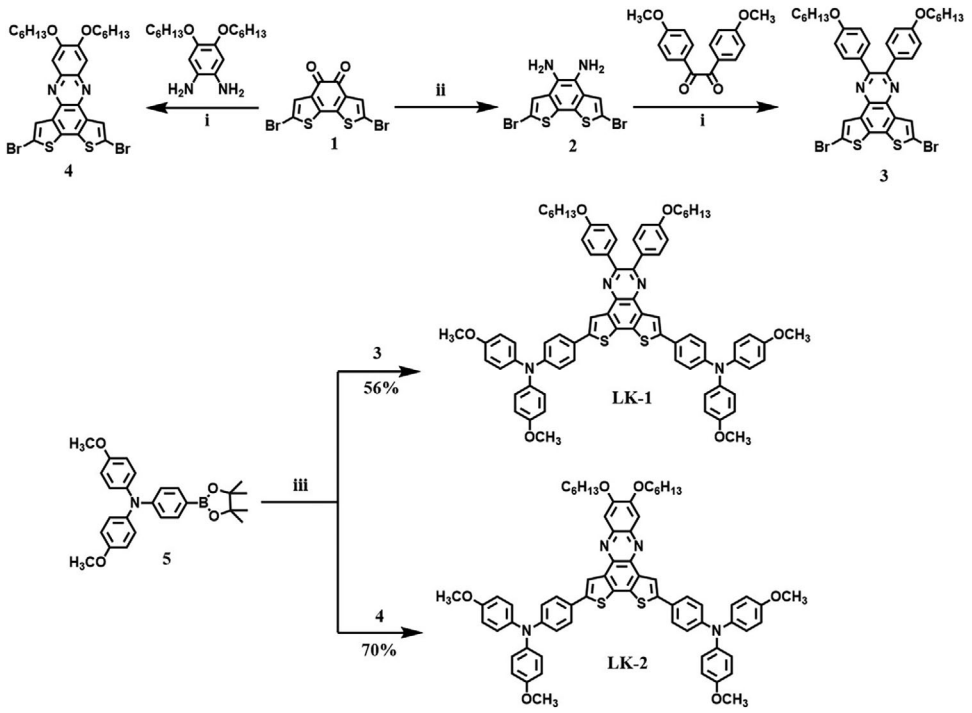

Scheme 1. Synthetic routes of **LK-1** and **LK-2**. i) EtOH, reflux; ii) NH_2OH, Pd/C, NH_2NH_2; iii) $Pd(PPh_3)_4$, 2 M K_2CO_3, toluene.

Table 1. Electro–optical properties of **LK-1** and **LK-2**.

HTM	λ_{max} [a] (nm)	λ_{em} [a] (nm)	E_{0-0} [b] (eV)	HOMO/LUMO (eV)	T_d [c] (°C)	μ [d] ($cm^2V^{-1}s^{-1}$)
LK-1	457	590	2.41	−5.05/−2.64	387	2.50×10^{-4}
LK-2	492	624	2.29	−4.99/−2.70	420	3.18×10^{-4}

[a] Absorption and emission spectra were measured in dichloromethane at a concentration of 1.0×10^{-5} M. [b] E_{0-0} was determined from the intersection of absorption and emission spectra. [c] T_d: thermal decomposition temperature. [d] Hole mobilities of HTMs.

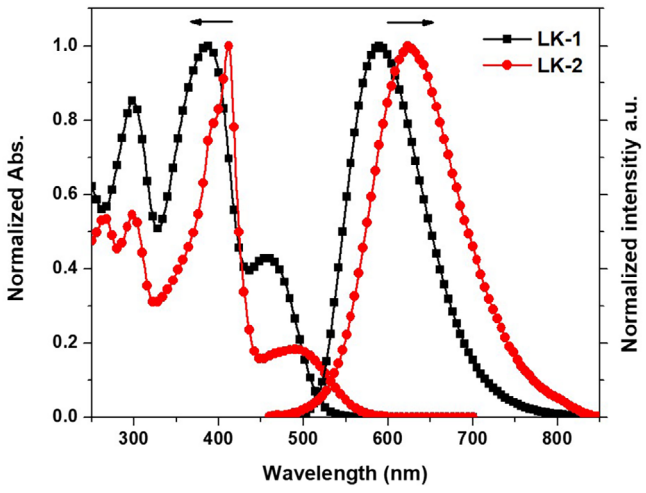

Figure 1. The absorption and emission spectra of **LK-1** and **LK-2**.

2.3. Electrochemical Properties

The electrochemical properties and energy levels of **LK-1** and **LK-2** were investigated by cyclic voltammetry experiments in dichloromethane solution and related data were summarized in Table 1. As shown in Figure 2a, **LK-1** and **LK-2** exhibited quasi-reversible redox curve, showing their good electrochemical stability. The energy level diagrams of the LK series compound in relation to a PSC are illustrated in Figure 2b. The HOMO levels of **LK-1** and **LK-2** were calculated to be −5.05 and −4.99 eV, respectively. These values are slightly higher than the HOMO level of the perovskite layer (−5.43 eV), indicating that both **LK-1** and **LK-2** are suitable as hole transport materials for extracting holes from the perovskite layer. Furthermore, the LUMO levels of **LK-1** and **LK-2** were found to be −2.64 and −2.70 eV, respectively. These LUMO levels are higher than the conduction band of the perovskite layer (−3.92 eV), which effectively prevents electrons from being transferred to the hole transport layer, thereby minimizing interference with the operation of the solar cell. Overall, the energy level alignment of **LK-1** and **LK-2** with

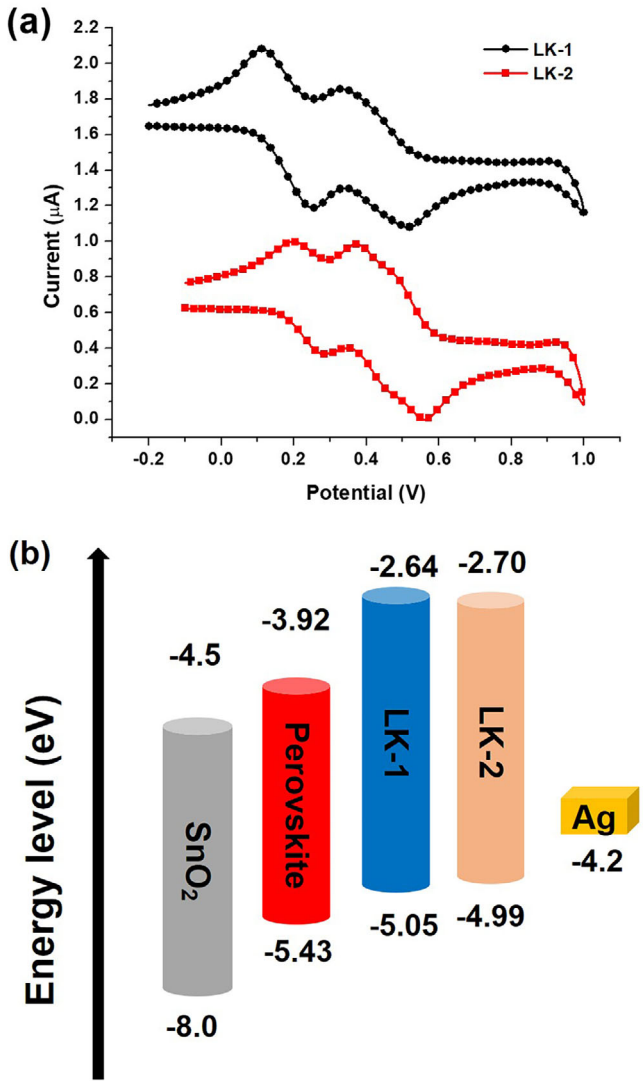

Figure 2. a) Cyclic voltammetry curve of **LK-1** and **LK-2**. b) Schematic energy levels of HTMs and perovskite.

the perovskite layer suggests their potential as efficient hole transport materials in PSCs.

2.4. Thermal Stability

Thermogravimetric analysis (TGA) revealed distinct thermal decomposition profiles for the hole transport materials (HTMs) **LK-1** and **LK-2**. The TGA of **LK-1** and **LK-2** was carried out, relevant spectra are shown in Figure S2, and the data are listed in Table 1. The thermal decomposition temperature (T_d), defined as the temperature at which a 5% weight loss occurs, was measured at 387 °C for **LK-1** and 420 °C for **LK-2** (Table 1). The superior T_d of **LK-2** compared to **LK-1** suggests enhanced molecular stability, likely due to structural modifications that mitigate bond dissociation at elevated temperatures. The DSC curves (Figure S3) showed that the glass-transition temperature (Tg) of **LK-1** and **LK-2** were 100 and 108 °C, respectively. The results demonstrate that both

HTM	HOMO	LUMO
LK-1	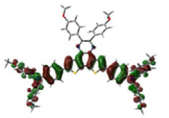	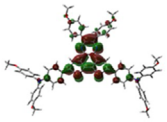
LK-2	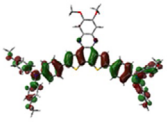	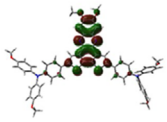

Figure 3. HOMO and LUMO distributions of **LK-1** and **LK-2**.

LK-1 and **LK-2** HTMs exhibit good thermal stability, satisfying the thermal requirements in PSCs under continuous illumination.

2.5. Theoretical Computation

To elucidate molecular orbital distributions and electronic structures, computational studies were performed using Gaussian 16 W with density functional theory (DFT) at the B3LYP/6-31G(d) basis set. The OC_6H_{13} substituents in **LK-1** and **LK-2** were replaced with OCH_3 to simplify the computation process. Optimized molecular geometries and related frontier orbital (HOMO and LUMO) distributions are displayed in Figures S4 and 3. The optimized geometries of **LK-1** and **LK-2** revealed planar configurations in their conjugated cores (Figure S4), a feature conducive to intermolecular π–π stacking interactions. The HOMOs of **LK-1** and **LK-2** localized predominantly on the electron-donating 4,4-dimethoxy-triphenylamine moieties, extending partially into the core structures. In contrast, the LUMOs of both molecules concentrated on the core regions, with partial overlap between HOMO and LUMO distributions indicative of ICT characteristics. Calculated HOMO energies for **LK-1** and **LK-2** were −4.50 and −4.44 eV, respectively, whereas LUMO energies measured −1.87 eV (**LK-1**) and −1.99 eV (**LK-2**). The lower LUMO energy of **LK-2** correlates with its stronger electron-withdrawing core, which enhances stabilization of the unoccupied orbitals. Bandgap analysis showed **LK-2** (2.45 eV) possessed a narrower energy gap compared to **LK-1** (2.63 eV), consistent with electrochemical measurements.

2.6. Morphology

The scanning electron microscopy (SEM) images provide detailed insights into the surface morphology of different HTMs, including spiro-OMeTAD, **LK-1**, and **LK-2**, when coated on the perovskite (PVSK) layer. As shown in Figure 4, the surface of the **LK-1** coated film shows observable pinhole and some particles, indicating less uniform coating over the perovskite layer. In contrast, **LK-2** exhibits better film-forming properties, resulting in a more uniform morphology than **LK-1** but slightly less smooth than spiro-OMeTAD. The absence of significant pinholes or voids

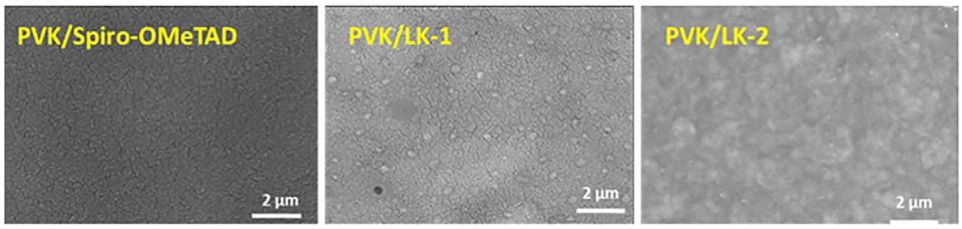

Figure 4. Top-view SEM images of PVK/spiro-OMeTAD, PVK/**LK-1** and PVK/**LK-2**.

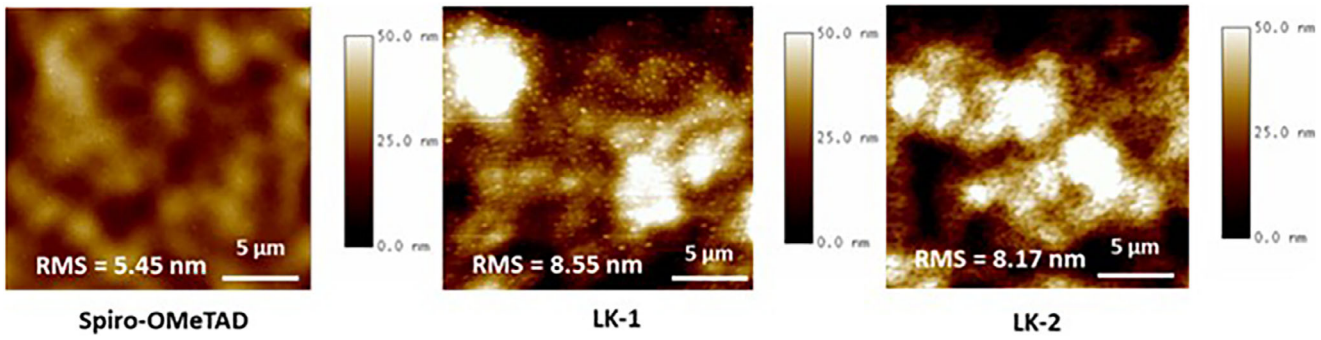

Figure 5. AFM images of PVK/spiro-OMeTAD, PVK/**LK-1**, and PVK/**LK-2**.

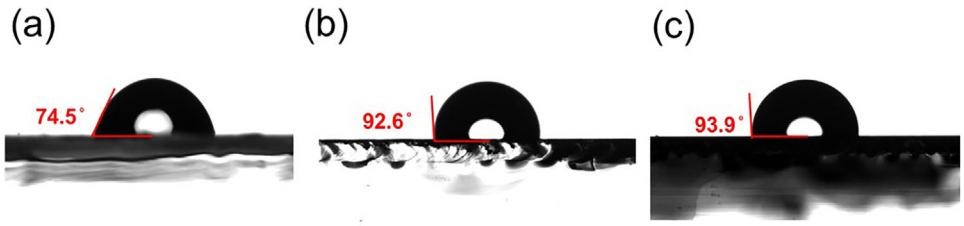

Figure 6. Water contact angles of a) spiro-OMeTAD, b) **LK-1**, and c) **LK-2**.

in the perovskite film suggests good material quality, which is essential for efficient charge transport and reduced recombination losses. To further quantify the surface morphology, AFM analysis was conducted to evaluate the roughness of spiro-OMeTAD, **LK-1**, and **LK-2** films deposited on the perovskite layer. As shown in Figure 5, the root mean square (RMS) roughness values of spiro-OMeTAD, **LK-1**, and **LK-2** were 5.45, 8.55, and 8.17 nm, respectively. The results indicate that **LK-2** has a smoother surface compared to **LK-1**, with a lower RMS roughness value. A smoother HTM layer is beneficial for reducing interfacial charge scattering, enhancing hole extraction, and improving overall device efficiency. The operational longevity of PSCs is critically contingent upon the judicious selection of HTMs that exhibit robust hydrophobic characteristics. Water contact angle measurements revealed that **LK-1** and **LK-2** exhibited contact angles of 92.6° and 93.9° (Figure 6), respectively, which are higher than that of the standard spiro-OMeTAD (74.5°). This indicates that both **LK1** and **LK-2** possess enhanced hydrophobicity compared to spiro-OMeTAD. Such an augmented hydrophobicity is posited to confer a formidable barrier against the ingress of ambient moisture, thereby effectively preempting the hydrolytic degradation of the perovskite absorber layer.

2.7. Device Performance

To investigate the photovoltaic performance of **LK-1** and **LK-2**, we fabricated in the n-i-p architecture of PSCs with FTO/SnO_2/$Cs_{0.05}MA_{0.2}FA_{0.75}Pb(Br_{0.05}I_{0.95})_3$/HTM/Ag device configuration, using **LK-1** and **LK-2** as HTM. The detailed fabrication of PSCs device was described in the Supporting Information. The *J*–*V* curves of PSCs based on **LK-1** and **LK-2** as HTM under AM 1.5 G illumination are shown in Figure 7a and the data are listed in Table 2. For **LK-1**, the champion device demonstrated a J_{SC} of 23.92 mA/cm^2 and a V_{OC} of 1.041 V, resulting in a fill factor of 72.65% and a PCE of 18.16%. By contrast, **LK-2** exhibited the highest performance a V_{OC} of 1.085 V, J_{SC} of 24.39 mA/cm^2, an FF of 72.87%, and a PCE of 19.40%, surpassing **LK-1** in both V_{OC} and J_{SC}, indicating improved charge transport properties and reduced recombination losses. Under the same illumination conditions, the efficiency of **LK-2** is comparable to that of PSC devices using spiro-OMeTAD as the HTM (J_{SC} = 24.69 mA/cm^2, V_{OC} = 1.15 V, FF = 76.77%, and PCE = 21.81%). The superior characteristics of **LK-2** suggest it has greater potential for high-efficiency applications in PSCs. Figure 7b illustrates the external quantum efficiencies

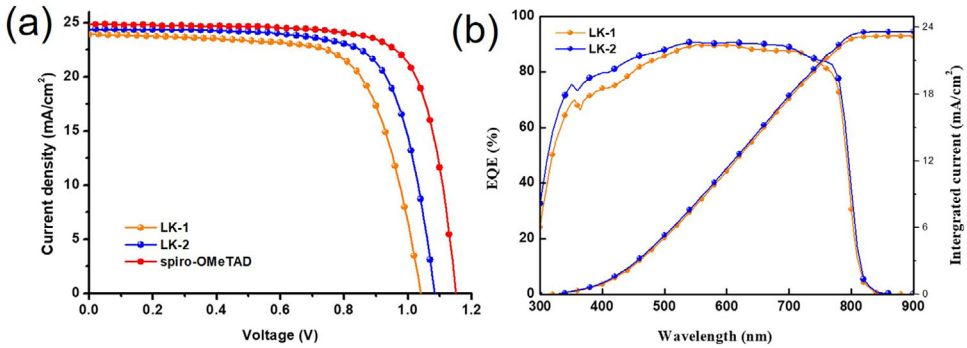

Figure 7. a) *J*–*V* curve. b) EQE spectra of **LK-1** and **LK-2** based PSCs.

Table 2. Photovoltaic parameter of PSCs fabricated with **LK-1** and **LK-2** as HTM.

HTM	J_{SC} (mA/cm^2)	V_{OC} (*V*)	FF (%)	PCE (%)
LK-1	23.92 (Forward)	1.040	72.65	18.16
	23.89 (Reverse)	1.037	70.89	17.72
	23.61 ± 0.19[a)]	0.930 ± 0.019	71.91 ± 1.21	15.81 ± 0.44
LK-2	24.39 (Forward)	1.085	72.87	19.40
	24.38 (Reverse)	1.083	72.46	19.26
	24.26 ± 0.15	1.070 ± 0.014	72.32 ± 1.49	18.80 ± 0.37
Spiro-OMeTAD	24.84 (Forward)	1.151	75.59	21.61
	24.69 (Reverse)	1.151	76.77	21.81
	24.03 ± 0.32	1.103 ± 0.017	73.51 ± 0.67	19.48 ± 0.44

[a)] The average values were calculated based on 10 PVSC devices.

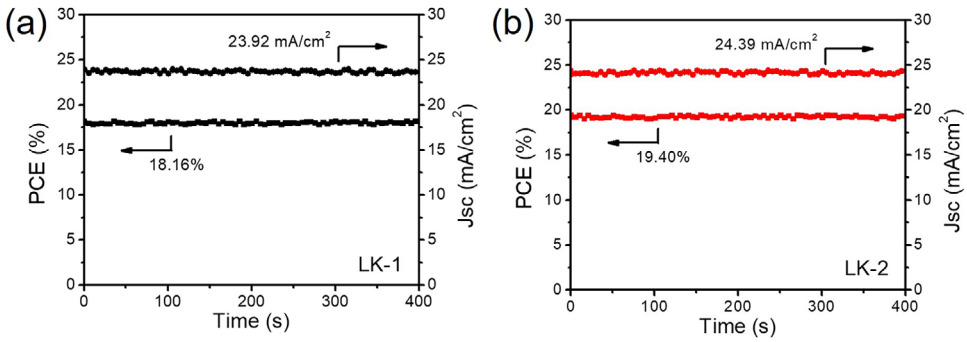

Figure 8. Stabilized power output of PSC devices for a) **LK-1** and b) **LK-2**-based PSCs at their maximum power point.

(EQEs) spectra acquired from the perovskite devices. The EQE spectra for the **LK-1** and **LK-2** HTMs demonstrate a wide spectral response, spanning from 350 to 750 nm. The integrated photocurrent densities were calculated to be 23.18 and 23.60 mA cm^{-2} from the EQE spectra, respectively, which are consistent with the J_{SC} values derived from the *J*–*V* curve. To validate the *J*–*V* curve measurements, the devices using **LK-1** and **LK-2** were tested for stabilized PCE at their maximum power point (Figure 8). The results exhibited that the devices based on **LK-1** and **LK-2** have stable PCEs of 18.16% and 15.39%, respectively. The hysteresis characteristics of the fabricated devices were assessed by performing forward and reverse scans of the current density–voltage (*J*–*V*) curves (Figure S5). The results revealed that the devices incorporating **LK-1** and **LK-2** exhibited negligible hysteresis effect with calculated hysteresis index of 2.4% (**LK-1**) and 0.7% (**LK-2**), which indicates reducing the trap-assisted charge recombination[52] by **LK-1** and **LK-2** defect passivation. This can be attributed to the enhanced hole mobility and more efficient interfacial charge transport associated with these two HTMs, thereby facilitating a more balanced hole/electron charge transfer dynamic.

The hole mobility of the HTM serves as an intuitive parameter to evaluate its hole transport ability. To gain deeper insights into the charge transport characteristics of **LK-1** and **LK-2**, we employed the space-charge-limited current (SCLC) method to investigate the hole mobility using the hole-only device with a configuration of FTO/PEDOT:PSS/HTM/Ag structure without any additives. The corresponding current–voltage spectra are

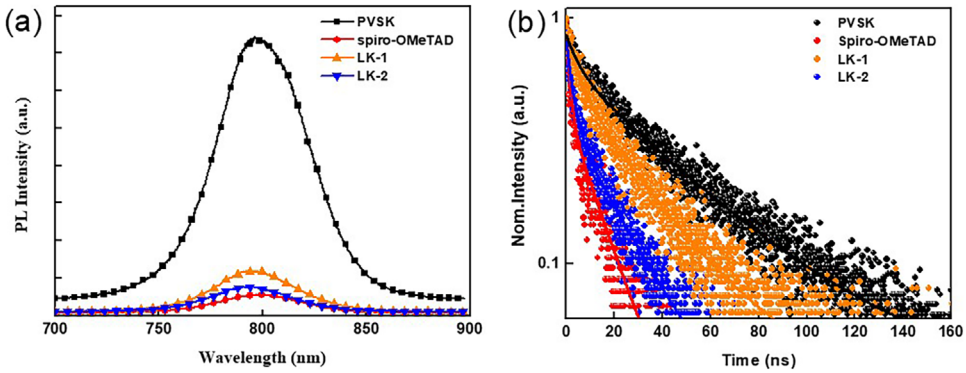

Figure 9. a) Steady-state PL spectra of perovskite and b) time-resolved PL spectra of perovskite with **LK-1**, **LK-2**, and spiro-OMeTAD.

revealed in Figure S6. Specifically, **LK-1** exhibited a hole mobility of 2.5 × 10^{-4} cm^2 V^{-1} s^{-1}, whereas **LK-2** demonstrated a slightly higher hole mobility of 3.18 × 10^{-4} cm^2 V^{-1} s^{-1}, which is comparable to that of spiro-OMeTAD (3.07 × 10^{-4} cm^2 V^{-1}). This increase in hole mobility for **LK-2** suggests an enhanced capability for hole extraction and transport within the PSC architecture. The superior hole mobility of **LK-2** is consistent with its observed higher J_{SC} and V_{OC} in the full photovoltaic devices, indicating a direct correlation between improved charge carrier transport properties and enhanced device performance.

In order to investigate the charge transfer dynamics at the perovskite interface and to assess the efficiency of hole extraction by **LK-1** and **LK-2**, we carried out the steady-state photoluminescence (PL) measurements. The measurements provided further insights into the charge transfer properties of **LK-1** and **LK-2**. As shown in Figure 9a, the results revealed that perovskite surfaces coated with **LK-2** exhibited more pronounced PL quenching compared to those coated with **LK-1**. This suggests that **LK-2** facilitates more efficient charge extraction and transfer, leading to reduced recombination at the perovskite interface. The enhanced PL quenching efficiency observed for **LK-2** aligns well with its performance in photovoltaic measurements, reinforcing its capability to serve as an effective hole transport material. To further analyze charge carrier dynamics, time-resolved photoluminescence (TRPL) measurements were performed to evaluate carrier lifetime and recombination behavior in perovskite films coated with different HTMs.[53] The TRPL spectra are shown in Figure 9b and the relevant data are listed in Table S1. The TRPL spectra curves revealed distinct variations in charge carrier lifetimes depending on the HTM used. By fitting the TRPL decay profiles with the biexponential function,[54] in which fast decay (τ_1) mainly corresponds to charge extraction from the perovskite to the HTMs, and slow decay (τ_2) is attributed to interface charge recombination losses. Both of these two HTMs show faster decay lifetime (τ_1 and τ_2) than the pristine perovskite film. The perovskite films coated with **LK-1** exhibited longer carrier lifetimes (τ_{avg} = 17.64 ns) compared to those with **LK-2** (τ_{avg} = 9.99 ns) and the reference spiro-OMeTAD (τ_{avg} = 6.73 ns). The shorter carrier lifetime observed for **LK-2** suggests more efficient charge extraction from perovskite to **LK-2**, which is consistent with its larger steady-state PL quenching and superior photovoltaic performance. These results further confirm that **LK-2** is a more effective HTM, contributing to enhanced charge transport and overall device performance. On the other hand, although the hole mobility of **LK-2** is comparable to that of spiro-OMeTAD, TRPL lifetime measurements show that spiro-OMeTAD has a shorter lifetime than **LK-2** when coated on the perovskite. This suggests that spiro-OMeTAD likely has a more efficient charge extraction capability, which in turn leads to its higher PCE compared to **LK-2**. In order to get more insight into the charge dynamic and recombination between the interface of the HTM and perovskite, the light intensity-dependent performance of PSCs **LK-1** and **LK-2** was investigated through variable light intensity measurements (Figure 10). The results revealed the J_{SC} exhibited a linear relationship with light intensity (Figure 10a), and the slopes for **LK-1**, **LK-2,** and the spiro-OMeTAD control device are 0.921, 0.945, and 0.924, respectively. This shows that the charge collection efficiency is independent of light intensity and that the space-charge recombination at the HTL/perovskite interface is negligible.[55] Furthermore, the analysis of the V_{OC} versus light intensity revealed significant differences in the recombination mechanisms between the two devices. The observed slope of 1.76 for **LK-1** and 1.67 for **LK-2** (Figure 10b) indicates a suppression of Shockley–Read–Hall trap-assisted carrier recombination in **LK-2** compared to **LK-1**,[56] which is in agreement with an improved V_{OC}.

To further elucidate the correlation between enhanced hydrophobicity and the long-term operational stability of PSCs in humid environments, the stability of unencapsulated devices featuring different HTMs was evaluated under an ambient atmosphere with 40%–50% relative humidity. As shown in Figure 11a, devices employing **LK-1** and **LK-2** retained 80% and 86% of their initial PCEs, respectively, whereas devices with spiro-OMeTAD showed a more pronounced decline, retaining only 71%. These results indicate that **LK-1** and **LK-2** possess superior stability under moderate humidity, consistent with their enhanced hydrophobicity as demonstrated by their higher water contact angles. This suggests that the improved moisture barrier effect contributes to their better environmental stability. To further examine the thermal durability of the HTMs, devices were subjected to continuous heating at 85 °C in a nitrogen atmosphere. After 1000 h, **LK-1** and **LK-2** retained 64% and

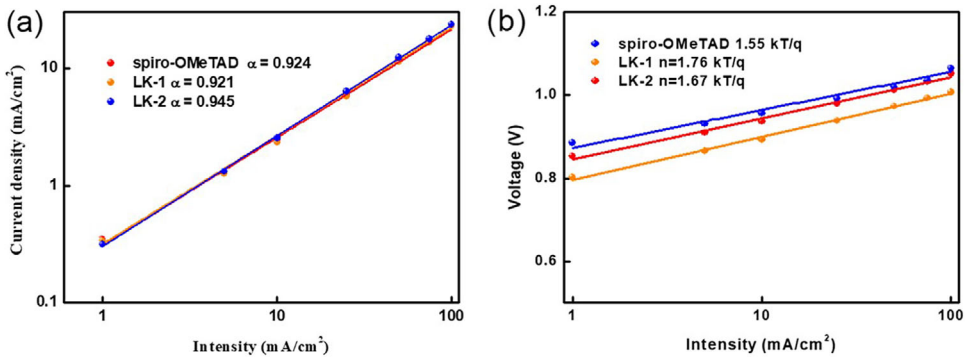

Figure 10. a) Light intensity dependency of J_{SC} and b) of V_{OC} with **LK-1** and **LK-2**.

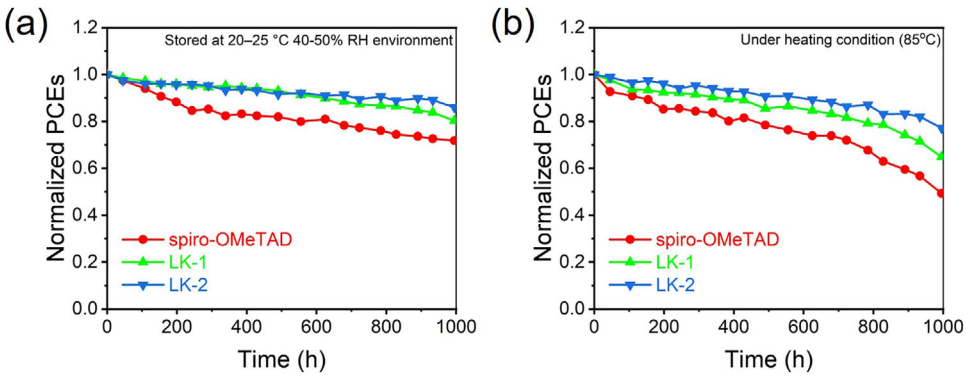

Figure 11. a) The stability test of the unencapsulated device stored at 20–25 °C and b) thermal aging at 85 °C.

77% of their original PCEs, respectively, whereas spiro-OMeTAD dropped significantly to 49% (Figure 11b). These findings are in line with the TGA and differential scanning calorimetry (DSC) results, indicating excellent thermal stability.

3. Conclusions

In summary, two novel HTMs, **LK-1** and **LK-2**, based on dithieno[3,2-*f*:2′,3′-*h*]quinoxaline (DTQu) and dithieno[3,2-*a*:2′,3′-*c*]phenazine (DTPh) cores, were successfully synthesized and characterized for application in PSCs. The results demonstrate that both materials exhibit promising properties, including suitable energy level alignment with the perovskite layer, high thermal stability, and efficient charge transport capabilities. Among the two HTMs, **LK-2** outperformed **LK-1** in photovoltaic performance, achieving PCE of 19.40%, compared to 18.16% for **LK-1**. This superior performance is attributed to **LK-2**'s enhanced charge transport properties, reduced recombination losses, and better interfacial charge transfer dynamics. Additionally, **LK-2** demonstrated improved hysteresis behavior and more efficient PL quenching, further highlighting its potential as a high-performance HTM. The findings of this study underscore the importance of molecular design in developing advanced HTMs for PSCs. The incorporation of rigid and planar fused-heterocyclic cores, such as DTQu and DTPh, provides a versatile platform for optimizing electronic properties, improving device stability, and enhancing charge transport efficiency. These results pave the way for further exploration of D–A–D structured HTMs to achieve higher efficiencies and long-term operational stability in PSCs. We foresee that by employing the strategies such as focusing on fine-tuning the molecular structure through functionalization and side-chain engineering to optimize energy levels, enhance charge transport, improve film morphology, and maximize defect passivation, we believe the performance of quinoxaline-based HTMs can be further improved to achieve efficiencies competitive with or exceeding that of conventional spiro-OMeTAD.

4. Experimental Section

The detailed synthesis procedure, characterizations, computational results, and PSCs device fabrication process are provided in the Supporting Information.

Acknowledgments

This work was financially supported by the National Science and Technology Council of Taiwan (NSTC 113-2113-M-033-006). The authors also acknowledge the Research Core Facility at National Central University for providing high resolution mass spectrometry.

Conflict of Interests

The authors declare no conflict of interest.

Data Availability Statement

The data that support the findings of this study are available on request from the corresponding author. The data are not publicly available due to privacy or ethical restrictions.

Keywords: Dithienoheterocycle · Donor–acceptor–donor (D–A–D) · Hole mobility · Hole transporting materials · Perovskite solar cells (PSC)

[1] A. S. R. Bati, Y. L. Zhong, P. L. Burn, M. K. Nazeeruddin, P. E. Shaw, M. Batmunkh, *Commun. Mater.* **2023**, *4*, 2.
[2] P. Xiao, K. Ding, J. Yang, P. Yu, L. Yang, X. Zhang, D. Guo, L. Sun, J. Shao, Z. Zhuang, M. Zhu, Y. Miao, *Chem. Asian J.* **2025**, *20*, e202401816.
[3] P. Xiao, M. Zhang, X. Wu, K. Ding, J. Pan, J. Jie, *Sol. Ener.* **2022**, *234*, 111–118.
[4] Z. Liang, Y. Zhang, H. Xu, W. Chen, B. Liu, J. Zhang, H. Zhang, Z. Wang, D.-H. Kang, J. Zeng, X. Gao, Q. Wang, H. Hu, H. Zhou, X. Cai, X. Tian, P. Reiss, B. Xu, T. Kirchartz, Z. Xiao, S. Dai, N.-G. Park, J. Ye, X. Pan, *Nature* **2023**, *624*, 557–563.
[5] H. Wang, Y. Zheng, G. Zhang, P. Wang, X. Sui, H. Yuan, Y. Shi, G. Zhang, G. Ding, Y. Li, T. Li, S. Yang, Y. Shao, *Adv. Mater.* **2024**, *36*, 2307855.
[6] F. Wang, T. Wang, Y. Sun, X. Liang, G. Yang, Q. Li, Y. Li, X. Zhou, Q. Zhu, A. Ng, H. Lin, M. Yuan, Y. Shi, T. Wu, H. Hu, *Adv. Mater.* **2024**, *36*, 2401476.
[7] F. Ma, Y. Zhao, Z. Qu, J. You, *Acc. Mater. Res.* **2023**, *4*, 716–725.
[8] L. Calio, S. Kazim, M. Gratzel, S. Ahmad, *Angew. Chem., Int. Ed. Engl.* **2016**, *55*, 14522–14545.
[9] K. M. Anoop, T. N. Ahipa, *Sol. Ener.* **2023**, *263*, 111937.
[10] A. Farokhi, H. Shahroosvand, G. D. Monache, M. Pilkington, M. K. Nazeeruddin, *Chem. Soc. Rev.* **2022**, *51*, 5974–6064.
[11] P. Murugan, T. Hu, X. Hu, Y. Chen, *J. Mater. Chem. A* **2022**, *10*, 5044–5081.
[12] H. D. Pham, T. C.-J. Yang, S. M. Jain, G. J. Wilson, P. Sonar, *Adv. Ener. Mater.* **2020**, *10*, 1903326.
[13] P. Yan, D. Yang, H. Wang, S. Yang, Z. Ge, *Ener. Environ. Sci.* **2022**, *15*, 3630–3669.
[14] G. B. Adugna, K.-M. Lee, H.-C. Hsieh, S.-I. Lu, C.-H. Lin, Y.-C. Hsieh, J. H. Yang, J.-M. Chiu, Y.-S. Liu, C.-W. Hu, W.-H. Chiu, S.-R. Li, K.-L. Liau, Y.-T. Tao, Y.-D. Lin, *Sol. RRL* **2024**, *8*, 2300988.
[15] K.-M. Lee, C.-H. Lin, C.-C. Chang, T.-Y. Yang, W.-H. Chiu, W.-C. Chu, Y.-H. Chang, S.-R. Li, S.-I. Lu, H.-C. Hsieh, K.-L. Liau, C. H. Hu, C.-H. Chen, Y.-S. Liu, W.-C. Chou, M. M. Lee, S.-S. Sun, Y.-T. Tao, Y.-D. Lin, *Adv. Sci.* **2025**, *12*, 2410666.
[16] K.-M. Lee, Y.-S. Huang, W.-H. Chiu, Y.-K. Huang, G. Chen, G. B. Adugna, S.-R. Li, F.-J. Lin, S.-I. Lu, H.-C. Hsieh, K.-L. Liau, C.-C. Huang, Y. Tai, Y.-T. Tao, Y.-D. Lin, *Adv. Funct. Mater.* **2023**, *33*, 2306367.
[17] F. Yang, D. Jang, L. Dong, S. Qiu, A. Distler, N. Li, C. J. Brabec, H.-J. Egelhaaf, *Adv. Ener. Mater.* **2021**, *11*, 2101973.
[18] L. Zhang, X. Zhou, C. Liu, X. Wang, B. Xu, *Small Methods* **2020**, *4*, 2000254.
[19] Y. Shen, K. Deng, L. Li, *Small Methods* **2022**, *6*, 2200757.
[20] S.-Y. Jeong, H.-S. Kim, N.-G. Park, *ACS Appl. Mater. Interfaces* **2022**, *14*, 34220–34227.
[21] L. Nakka, Y. Cheng, A. G. Aberle, F. Lin, *Adv. Ener. Sustain. Res.* **2022**, *3*, 2200045.
[22] J.-Y. Seo, S. Akin, M. Zalibera, M. A. R. Preciado, H.-S. Kim, S. M. Zakeeruddin, J. V. Milić, M. Grätzel, *Adv. Funct. Mater.* **2021**, *31*, 2102124.
[23] S. Venkateswarlu, Y.-D. Lin, K.-M. Lee, K.-L. Liau, Y.-T. Tao, *ACS Appl. Mater. Interf.* **2020**, *12*, 50495–50504.
[24] K. Manda, V. D. Jadhav, P. Chetti, R. Gundla, S. Pola, *Org. Electron.* **2025**, *136*, 107153.
[25] J. Santos, J. Calbo, R. Sandoval-Torrientes, I. García-Benito, H. Kanda, I. Zimmermann, J. Aragó, M. K. Nazeeruddin, E. Ortí, N. Martín, *ACS Appl. Mater. Interf.* **2021**, *13*, 28214–28221.
[26] J. Wagner, R. D. Chavan, J. Kruszyńska, M. Ans, A. Mahapatra, N. Mrkyvkova, P. Siffalovic, P. Yadav, M. Ebic, S. Akin, A. Kubas, M. Lindner, D. Prochowicz, *ACS Appl. Mater. Interf.* **2024**, *16*, 64940–64950.
[27] G. Xie, J. Wang, S. Yin, A. Liang, W. Wang, Z. Chen, C. Feng, J. Yu, X. Liao, Y. Fu, Q. Xue, Y. Min, X. Lu, Y. Chen, *Angew. Chem., Int. Ed. Engl.* **2024**, *63*, e202403083.
[28] D. Chandrasekaran, Y. L. Chiu, C. K. Yu, Y. S. Yen, Y. J. Chang, *Chem. Asian J.* **2021**, *16*, 3719–3728.
[29] D. Chandrasekaran, S.-J. Liou, W.-H. Chiu, L.-C. Lee, K.-M. Lee, Y.-C. Wu, H.-H. Chou, Y. J. Chang, Y.-S. Yen, *J. Power Sources* **2023**, *581*, 233496.
[30] Y. J. Chang, N.-H. Chen, T. Y. Chen, Y. M. Shuang, Y.-S. Yen, *ACS Appl. Ener. Mater.* **2024**, *7*, 1287–1297.
[31] P. Meti, H.-H. Park, Y.-D. Gong, *J. Mater. Chem. C* **2020**, *8*, 352–379.
[32] A. M. Shaikh, B. K. Sharma, S. Chacko, R. M. Kamble, *RSC Adv.* **2016**, *6*, 94218–94227.
[33] H. Guo, H. Zhang, C. Shen, D. Zhang, S. Liu, Y. Wu, W.-H. Zhu, *Angew. Chem., Int. Ed. Engl.* **2021**, *60*, 2674–2679.
[34] H. H. Jo, H.-J. Lee, J. Kang, S. Y. Kim, S.-I. Na, K. Zong, *Dyes Pigm.* **2025**, *239*, 112722.
[35] Y.-S. Lin, N.-H. Chen, C.-M. Liu, T. J. Chow, C.-P. Chen, Y. J. Chang, *Sol. RRL* **2023**, *7*, 2300692.
[36] Z. Wang, C. Xu, Z. Yang, Y. Zou, K. Zhang, P. Gao, W. Xu, G. Li, J. Chen, M. Liang, *Dyes Pigm.* **2023**, *211*, 111066.
[37] L. Fang, Y. Zhang, M. Ren, X. Xie, T. Li, Y. Yuan, J. Zhang, P. Wang, *Ener. Environ. Sci.* **2022**, *15*, 1630–1637.
[38] K. Zhao, Q. Liu, L. Yao, C. Değer, J. Shen, X. Zhang, P. Shi, Y. Tian, Y. Luo, J. Xu, J. Zhou, D. Jin, S. Wang, W. Fan, S. Zhang, S. Chu, X. Wang, L. Tian, R. Liu, L. Zhang, I. Yavuz, H.-f. Wang, D. Yang, R. Wang, J. Xue, *Nature* **2024**, *632*, 301–306.
[39] Z. Xia, X. Feng, T. Wu, W. Zhang, C. Chen, L. Wang, W. Zhang, H. Wang, Y. Tian, Y. Hua, H. Chen, M. Cheng, *Adv. Funct. Mater.* **2024**, *34*, 2408423.
[40] Z. Yao, F. Zhang, L. He, X. Bi, Y. Guo, Y. Guo, L. Wang, X. Wan, Y. Chen, L. Sun, *Angew. Chem., Int. Ed. Engl.* **2022**, *61*, e202201847.
[41] F. Gao, Y. Zhao, X. Zhang, J. You, *Adv. Ener. Mater.* **2020**, *10*, 1902650.
[42] Y. Fu, Y. Li, G. Xing, D. Cao, *Mater. Today Adv.* **2022**, *16*, 100300.
[43] J. Y. Lee, S. Y. Kim, H. J. Yoon, *Adv. Opt. Mater.* **2022**, *10*, 2101361.
[44] W. Wang, J. Zhou, W. Tang, *J. Mater. Chem. A* **2022**, *10*, 1150–1178.
[45] X. Ji, T. Zhou, X. Ke, W. Wang, S. Wu, M. Zhang, D. Lu, X. Zhang, Y. Liu, *J. Mater. Chem. A* **2020**, *8*, 5163–5170.
[46] K. Yang, Q. Liao, J. Huang, Z. Zhang, M. Su, Z. Chen, Z. Wu, D. Wang, Z. Lai, H. Y. Woo, Y. Cao, P. Gao, X. Guo, *Angew. Chem., Int. Ed. Engl.* **2022**, *61*, e202113749.
[47] H. Zhang, X. Yu, M. Li, Z. Zhang, Z. Song, X. Zong, G. Duan, W. Zhang, C. Chen, W.-H. Zhang, Y. Liu, M. Liang, *Angew. Chem., Int. Ed. Engl.* **2023**, *62*, e202314270.
[48] Q. Cheng, H. Chen, F. Yang, Z. Chen, W. Chen, H. Yang, Y. Shen, X.-M. Ou, Y. Wu, Y. Li, Y. Li, *Angew. Chem., Int. Ed. Engl.* **2022**, *61*, e202210613.
[49] Q. Cheng, W. Chen, Y. Li, Y. Li, *Adv. Sci.* **2024**, *11*, 2307152.
[50] B. Mondal, R. Tiwari, S. Manna, F. Banerjee, R. Singh, S. K. Samanta, *ACS Appl. Ener. Mater.* **2025**, *8*, 3459–3469.
[51] F. A. Arroyave, C. A. Richard, J. R. Reynolds, *Org. Lett.* **2012**, *14*, 6138–6141.
[52] P. Liu, W. Wang, S. Liu, H. Yang, Z. Shao, *Adv. Ener. Mater.* **2019**, *9*, 1803017.
[53] A. A. B. Baloch, F. H. Alharbi, G. Grancini, M. I. Hossain, M. K. Nazeeruddin, N. Tabet, *J. Phys. Chem. C* **2018**, *122*, 26805–26815.
[54] D. Lu, G. Lv, Z. Xu, Y. Dong, X. Ji, Y. Liu, *J. Am. Chem. Soc.* **2020**, *142*, 11114–11122.
[55] D. Bi, S.-J. Moon, L. Häggman, G. Boschloo, L. Yang, E. M. J. Johansson, M. K. Nazeeruddin, M. Grätzel, A. Hagfeldt, *RSC Adv.* **2013**, *3*, 18762–18766.
[56] D. Glowienka, Y. Galagan, *Adv. Mater.* **2022**, *34*, 2105920.

Manuscript received: July 18, 2025
Revised manuscript received: August 1, 2025
Version of record online: ■■, ■■